

# Helium atmospheric pressure plasma jets touching dielectric and metal surfaces

Seth A. Norberg,<sup>1,a)</sup> Eric Johnsen,<sup>1,b)</sup> and Mark J. Kushner<sup>2,c)</sup>

<sup>1</sup>*Department of Mechanical Engineering, University of Michigan, 2350 Hayward Street, Ann Arbor, Michigan 48109-2125, USA*

<sup>2</sup>*Department of Electrical Engineering and Computer Science, University of Michigan, 1301 Beal Avenue, Ann Arbor, Michigan 48109-2122, USA*

(Received 18 May 2015; accepted 19 June 2015; published online 1 July 2015)

Atmospheric pressure plasma jets (APPJs) are being investigated in the context plasma medicine and biotechnology applications, and surface functionalization. The composition of the surface being treated ranges from plastics, liquids, and biological tissue, to metals. The dielectric constant of these materials ranges from as low as 1.5 for plastics to near 80 for liquids, and essentially infinite for metals. The electrical properties of the surface are not independent variables as the permittivity of the material being treated has an effect on the dynamics of the incident APPJ. In this paper, results are discussed from a computational investigation of the interaction of an APPJ incident onto materials of varying permittivity, and their impact on the discharge dynamics of the plasma jet. The computer model used in this investigation solves Poisson's equation, transport equations for charged and neutral species, the electron energy equation, and the Navier-Stokes equations for the neutral gas flow. The APPJ is sustained in He/O<sub>2</sub> = 99.8/0.2 flowing into humid air, and is directed onto dielectric surfaces in contact with ground with dielectric constants ranging from 2 to 80, and a grounded metal surface. Low values of relative permittivity encourage propagation of the electric field into the treated material and formation and propagation of a surface ionization wave. High values of relative permittivity promote the restrike of the ionization wave and the formation of a conduction channel between the plasma discharge and the treated surface. The distribution of space charge surrounding the APPJ is discussed. © 2015 AIP Publishing LLC.

[<http://dx.doi.org/10.1063/1.4923345>]

## I. INTRODUCTION

Atmospheric pressure plasma jets (APPJs) leverage a channel of noble gas created in air as a guide for an ionization wave (IW), the guided streamer, to deliver plasma produced activation energy to surfaces.<sup>1</sup> The resulting production of UV/VUV radiation, charged and reactive oxygen and nitrogen species (RONS) have motivated the use of APPJs for medical applications, from deactivation of bacteria to cancer treatment.<sup>2-7</sup> Recent investigations of APPJs have addressed surface functionalization<sup>8</sup> of various plastics, interaction with liquids,<sup>9,10</sup> and etching.<sup>11,12</sup> The parameters in these studies include the distance between the plasma jet and the surface (touching or not-touching), the adjacency of the electrical ground and the electrical properties of the surface being treating. These parameters, in turn, modify the characteristics of the APPJ, in some cases significantly affecting the plasma properties. For example, in recent experiments, the material of the target being treated by an APPJ was varied, with the result being a significantly different response of the plasma.<sup>13,14</sup> Recent computational investigations have also been conducted into the behavior of APPJs interacting with surfaces.<sup>15</sup>

The source of this sensitivity of APPJs to the electrical composition of the surface results, to first order, from the surface being an element in the electrical circuit of the APPJ. Power is applied to the electrodes of the APPJ through which current is delivered to the plasma. The current, in the form of conduction and/or displacement current, must return to electrical ground while conserving the total current through the circuit. Some of this current returns to ground through displacement current terminating on grounded surfaces surrounding the APPJ, and some of this current returns to ground through the surface being treated. If that surface is a dielectric, the current returning to ground through the surface charges its capacitance, which in turn reduces the voltage drop across the APPJ. This effect is the basis of the dielectric barrier discharge (DBD) in which virtually all the current returns to ground as displacement current through a dielectric.

In some applications of the APPJ treating a surface, the composition of the surface does not significantly vary from case to case. For example, the APPJ treatment of plastics for surface functionalization to modify the hydrophobic nature of the surface has a negligible effect on the bulk electrical properties of the material.<sup>16</sup> In other applications, the electrical properties of the surface may significantly vary from case to case. For example, in plasma medical applications, the permittivity of a wound can differ depending on the state of the wound during the healing process, and whether the wound is wet or dry.<sup>17,18</sup>

<sup>a)</sup>Present address: US Military Academy, Dept. of Civil and Mechanical Engr., West Point, NY 10996. Electronic mail: norbergs@umich.edu

<sup>b)</sup>ejohnsen@umich.edu

<sup>c)</sup>Author to whom correspondence should be addressed. Electronic mail: mjkhush@umich.edu

In this paper, we report on results of a computational investigation of an APPJ sustained in He/O<sub>2</sub> flowing into air which is incident onto a surface whose electrical properties are varied. The surface is a thin dielectric whose relative permittivity,  $\epsilon_r$ , is varied from 2 to 80, or is a metal. To simplify the investigation, we have assumed that the dielectric materials are ideal and so have zero electrical conductivity. The study is limited to a single discharge pulse onto each surface. The consequences of the electrical properties of the treated material on the properties of the APPJ are discussed. Through the high voltage portion of the pulse, high relative permittivity promotes a faster, more intense, ionization wave that leads to the formation of a more conductive channel between the pin electrode and the treated surface. The higher capacitance resulting from the higher  $\epsilon_r$  leads to more charging at the surface which results in a higher electric field at the surface of the material. The lower permittivity has a weaker ionization wave with less production of charged species and key neutrals within the conductive channel. However, the lower permittivity promotes penetration of the electric field into the material as well as the creation of a surface ionization wave (SIW).

Following a brief description of the model in Sec. II, characteristics of the APPJ onto surfaces having different electrical properties during and after a single discharge pulse are discussed in Sec. III. Concluding remarks are provided in Sec. IV.

## II. DESCRIPTION OF THE MODEL

The two-dimensional cylindrically symmetric model used for this computational investigation is *nonPDPSIM*, whose algorithms are discussed in Ref. 19. Briefly, *nonPDPSIM* is a plasma hydrodynamics model that solves Poisson's equation simultaneously with charged species transport using fully implicit techniques. Using time-slicing techniques, the electron energy equation with transport coefficients provided by solutions of Boltzmann equation for the electron energy distribution, neutral species transport equations, radiation transport and Navier-Stokes equations for bulk fluid transport are sequentially integrated. During the discharge pulses, time steps for modules vary from picoseconds for charged particle transport to hundreds of ps for fluid transport. The reaction mechanism discussed in Ref. 20, includes 51 neutral and charged species and 441 reactions.

The computational configuration uses an unstructured mesh and addresses a downward pointing plasma jet incident onto a surface of varying electrical composition. The computational domain is 19.5 mm by 8.8 mm, and has 7200 nodes of which 5400 are plasma nodes with various refinement zones as shown in Fig. 1. The unstructured, triangular mesh had spacing of 50  $\mu\text{m}$  at the tip of the electrode, 100  $\mu\text{m}$  at the surface of the dielectric, and 300  $\mu\text{m}$  in the periphery of the mesh. Experiments for APPJs have used confining tubes ranging from one to a few mm in diameter to nearly a centimeter in diameter, with flow rates ranging from a few slm to 15 slm of either helium or argon.<sup>21–24</sup> In this modeling investigation, the base case is a He/O<sub>2</sub> = 99.8/0.2 gas mixture at atmospheric pressure flowing through a 1.6 mm diameter tube at 4 slm. Although this geometry is intended to be

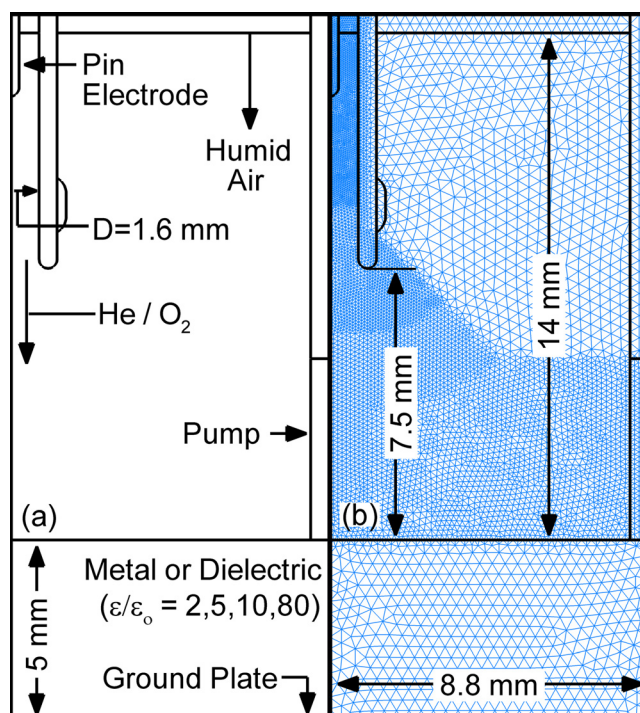


FIG. 1. Schematic of the cylindrically symmetric model geometry. (a) The full computational domain is 1.95 cm by 0.88 cm. (b) The numerical mesh with refinement zones.

representative of the general class of APPJs, the electrode orientation and dimensions were inspired by the kINPen developed by the INP Greifswald.<sup>24</sup> Humid air (N<sub>2</sub>/O<sub>2</sub>/H<sub>2</sub>O = 79.5/20/0.5) flows coaxially around the tube from the top surface at 4 slm to reduce the propensity for shear instabilities. All injected gases exit through a side port which is grounded. The material surface is 7.5 mm from the exit of the tube. The ring electrode has been treated as a dielectric for these simulations.

The electrical properties of the materials of the surface upon which the jet is incident were selected based on possible applications of APPJs. The relative permittivity ( $\epsilon_r = \epsilon/\epsilon_0$ ) of the material has values of  $\epsilon_r = 2, 5, 10$ , and 80, and metal. The low value of  $\epsilon_r = 2$  represents organic polymers, such as polyethylene ( $\epsilon_r = 2.25$ ) and fluorocarbon polymers, such as Teflon ( $\epsilon_r = 2.1$ ).<sup>25</sup> An intermediate value of  $\epsilon_r = 5$  was chosen to represent biological tissue.<sup>26</sup> An additional intermediate value of  $\epsilon_r = 10$  was chosen to represent materials, such as glass ( $\epsilon_r = 5-10$ ), graphite ( $\epsilon_r = 10-15$ ), and silicon ( $\epsilon_r = 11.7$ ).<sup>25,27</sup> Liquid water surfaces are represented by  $\epsilon_r = 80$ . The metal surface provides a reference. All non-metal materials had zero electrical conductivity. Treating tissue for wound healing by the ionization waves in APPJs is electrically similar to a floating dielectric barrier discharge with a poorly defined ground reached through the impedance of the patient. This situation, which varies from patient to patient, adds important variability to the process. This variability is, however, difficult to systematically address. In order to enable comparisons, we chose this simpler geometry. The thickness of the material was fixed at 5 mm in order to allow propagation of the electric field into the dielectric material prior to reaching the ground plate beneath the material.

### III. APPJ PROPERTIES DEPENDENT ON SURFACE COMPOSITION

In each case, the He/O<sub>2</sub> mixture was first flowed through the tube and into humid air to establish the flow field, typically for 8 ms. The steady state flow field is shown in Fig. 2 for He, O<sub>2</sub>, N<sub>2</sub>, and H<sub>2</sub>O. The average speed of the flow in the dielectric tube is 42 m/s corresponding to a Reynolds number of 630 indicating laminar flow.<sup>28</sup> After the profile was established, one  $-15$  kV pulse was applied to the pin electrode creating the discharge and launching an ionization wave. The voltage pulse has a 5 ns rise time, 75 ns duration at  $-15$  kV and a 20 ns fall time to zero for a total duration of 100 ns. There is no ballast resistance in series with the discharge. In each case, an ionization wave (IW) is launched at the pin electrode and propagates through the helium channel inside the tube, out of the tube into the ambient air and strikes the surface. The properties of the APPJ will be discussed early during the pulse when the ionization wave touches the surface, 10 ns after the IW touches the surface, 80 ns which is the end of the high voltage portion of the pulse, and 100 ns which is the time the voltage is terminated.

In summary, the electron avalanche quickly moves from the tip of the pin electrode to the inner wall of the discharge tube, charges the wall until the exit of the tube, and then moves on axis upon exiting the tube. The effluent is near room temperature; however, the *plasma bullet* is typically 2–3 eV in the head of the ionization wave<sup>29,30</sup> with an electron density ranging from  $1\text{--}2 \times 10^{13} \text{ cm}^{-3}$ .<sup>7</sup> The structure of the guided streamer is similar to a conventional atmospheric pressure streamer where space charge produced electric field enhancement in the head of the streamer generates an electron avalanche. The guided aspect of propagation results from the  $E/N$  (electric field/gas number density)

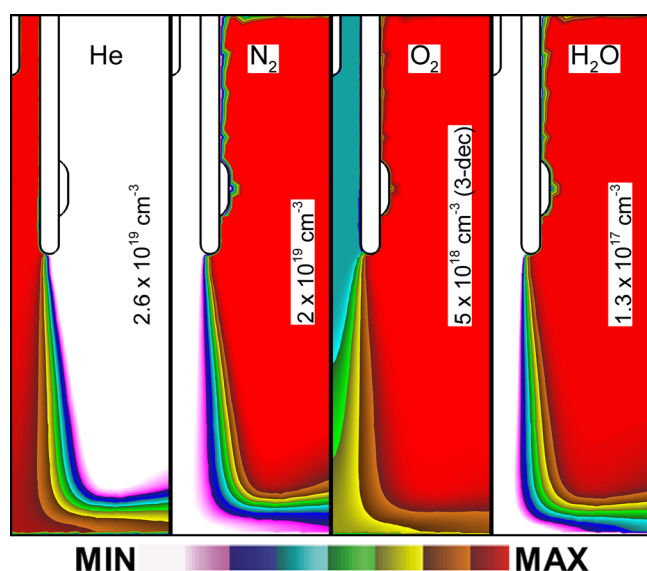


FIG. 2. He, N<sub>2</sub>, O<sub>2</sub>, and H<sub>2</sub>O concentrations for a flow rate of 4 slm He/O<sub>2</sub> = 99.8/0.2 through the tube prior to discharge ignition and humid air flowed as a shroud. Maximum values are shown in each frame (1 decade log scale). The O<sub>2</sub> concentration is plotted over three decades to highlight the 0.2% O<sub>2</sub> seeded in the He.

required for avalanche is lower in the rare-gas dominated plume than in the surrounding air. The avalanche is then prevented from spreading laterally into the air.

#### A. Touching the surface

As the guided ionization wave exits the dielectric tube, the spatial distribution of the electric field is determined by many factors. The space charge in the head of the IW produces the electric field that avalanches the streamer and sustains the IW. The axial electric field in the plasma column behind the IW is determined by the conductivity of the column. The radial electric field is determined by the effective ambipolar forces that confine the IW and, inside the tube, the charging of and dielectric properties of the tube itself. All of these properties are in turn sensitive to the proximity of the electrical ground and the capacitance (or dielectric properties) of solid materials between the IW and ground. The IW is a transient phenomenon and so the current from the metal of the powered electrode to the metal of the ground contains both conduction and displacement currents. The conduction current in large part resides from the electrode through the plasma column to the head of the IW. The current transitions from conduction to displacement current in the head of IW and continues as displacement current to the ground plane.

The dielectric properties of the materials between the IW and electrical ground affect the propagation of the IW in at least two ways. First, the continuity of the electric displacement vector,  $\vec{D} = \epsilon \vec{E}$  reapportions electric field magnitude from regions of larger  $\epsilon$  (here, solid material) into regions of smaller  $\epsilon$  (the gas and plasma). Second, when the conduction current of the IW and plasma column intersect with the solid dielectric, the solid electrically charges which in turn produces electric fields.

The electron temperature,  $T_e$ , electron impact ionization source,  $S_e$ , magnitude of the electric field,  $E$ , and electric potential contours are shown in Fig. 3 for ground-covering-dielectrics with relative permittivities of  $\epsilon_r = 2\text{--}80$  and for a metal substrate. The times of the images are when the IW touches the material. The speed of the ionization wave is indicated by the time of impact time shown in the figure. In general, the speed of the IW, the magnitude of the ionization source, and the peak electric field all increase with increasing  $\epsilon_r$  (and to the metal). The speed of the ionization waves increases from  $5.2 \times 10^7 \text{ cm s}^{-1}$  to  $6.8 \times 10^7 \text{ cm s}^{-1}$ ,  $S_e$  increases from  $5.2 \times 10^{20} \text{ cm}^{-3} \text{ s}^{-1}$  to  $2.5 \times 10^{21} \text{ cm}^{-3} \text{ s}^{-1}$ ,  $T_e$  increases from 5.3 eV to 6.3 eV and the electric field increases from 22 to 28 kV/cm (85 Td–110 Td, 1 Td =  $10^{-17} \text{ V cm}^2$ ) as  $\epsilon_r$  increases from 2 to 80. Prior to striking the surface, the increase in these quantities saturates by  $\epsilon_r = 80$ , with there being little difference in peak magnitudes and spatial distribution between  $\epsilon_r = 80$  and the metal surface.

The high permittivity materials create a large capacitance with no change to the surface area or distance to the electrode. Impedance, being inversely proportional to capacitance, decreases with increasing  $\epsilon_r$ . The lower impedance consumes a smaller fraction of the applied voltage, thereby increasing

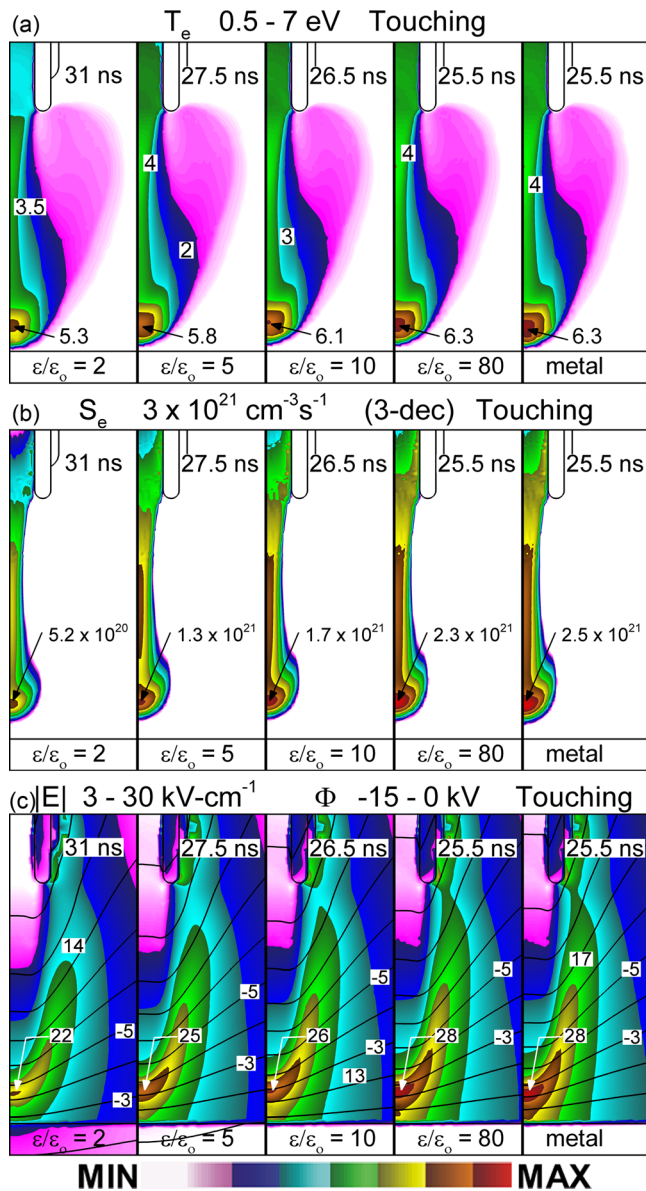


FIG. 3. Plasma dynamics at the time the ionization wave arrives at the material surface. Each case has He/O<sub>2</sub> = 99.8/0.2 flowing at 4 slm into humid air and a  $-15$  kV applied voltage. From left to right, the frames correspond to relative permittivities of 2, 5, 10, and 80, and metal. The time from beginning of the pulse to impact is listed for each permittivity. (a) Electron temperature  $T_e$ , (b) electron impact ionization source  $S_e$ , and (c) magnitude of the electric field with potential contours at  $-1$  kV intervals. The maximum value or range of values is noted in each figure.

the voltage across the electrode-to-dielectric gap relative to small  $\epsilon_r$ . From another perspective, high permittivity materials exclude electric fields, thereby displacing voltage into the gap. For  $\epsilon_r = 2$ , this effect is small, thereby enabling voltage contours to penetrate into the dielectric. The resulting smaller voltage across the gap produces an ionization wave that is 5.5 ns slower to the surface with an electron temperature 1 eV lower than for the high permittivity material. Increasing  $\epsilon_r$  to 5 produces an ionization wave that strikes the surface 3.5 ns earlier than for  $\epsilon_r = 2$  with a higher electron temperature, ionization source, and magnitude of electric field in the streamer head. At the time of impact, only for the  $\epsilon_r = 2$  case is there significant penetration of the electric field into the dielectric where the electric potential drop across the dielectric is

$>2$  kV. For  $\epsilon_r = 10$ , the penetration of potential into the material is less than 600 V.

## B. Touch + 10 ns

At the point at which the ionization wave just impacts the dielectric, only a small fluence of electrons has reached the surface and there is little charging of the surface. At 10 ns after the ionization wave strikes the dielectric, charging of the capacitance of the surface has occurred and continues to occur. This charging has significant feedback to the properties of the plasma plume. The ionization source term ( $S_e$ ), electron density ( $n_e$ ), total positive ion density ( $N_{tot}^+$ ), and total negative ion density ( $N_{tot}^-$ ) are shown in Fig. 4 for a time 10 ns after the IW strikes the surface. (Note that the absolute time is different for each material due to the difference in the speed of the IW.) The  $S_e$  responds in three distinctly different ways depending on the  $\epsilon_r$  of the dielectric. The first response is highlighted by the lower permittivity cases a few ns after impact. Here, the IW spreads across the surface and eventually splits from the vertical IW, forming a SIW. The SIW is sustained by horizontal components of the electric field at the surface of the dielectric. The  $S_e$  in the vertical column decreases and eventually terminates due to the charging of the surface which removes voltage from the gap. This is in some ways reminiscent of a DBD. The spreading phenomenon in DBDs can lead to self-organization of the plasma filaments.<sup>31,32</sup> The SIW increases in intensity for small increases in  $\epsilon_r$ . For example, the  $S_e$  in the SIW for  $\epsilon_r = 5$ ,  $3 \times 10^{20} \text{ cm}^{-3} \text{ s}^{-1}$  is commensurate with that in the plasma column,  $8 \times 10^{20} \text{ cm}^{-3} \text{ s}^{-1}$ .

The second response of  $S_e$  for larger  $\epsilon_r$  is a restrike in which a vertical IW travels back up the conductive plasma channel away from the surface. The intensity of the restrike depends on the effective capacitance of the material and increases with increasing  $\epsilon_r$ . With the increase in  $S_e$  in the restrike, the SIW decreases in intensity relative to the plasma column. The third response of  $S_e$  is the establishment of a conduction channel between the surface and the electrode at  $\epsilon_r = 80$  and for the metal substrate. This conduction channel coincides with the termination of the SIW. For example,  $S_e$  in the SIW for  $\epsilon_r = 80$ ,  $5 \times 10^{20} \text{ cm}^{-3} \text{ s}^{-1}$ , is small compared to that in the plasma column,  $6 \times 10^{21} \text{ cm}^{-3} \text{ s}^{-1}$ . For the metal surface,  $S_e$  in the plasma column is  $9 \times 10^{21} \text{ cm}^{-3} \text{ s}^{-1}$  with there being essentially no SIW due to the lack of a horizontal component of the electric field at the surface of the metal.

The dominance of the restrike or the SIW is largely a function of the charging of the dielectric. The SIW is sustained by horizontal components of the electric field produced by surface charging of the dielectric. This surface charging is at the expense of the vertical electric field and is the basis of operation of DBDs where voltage is removed from the gap prior to arcing. The smaller  $\epsilon_r$  and so smaller capacitance results in a smaller RC time constant for charging the surface, more rapid production of the horizontal component of the electric field that sustains the SIW and more rapid depletion of the vertical electric field. At the other extreme, with a metal substrate, there is no charging of the

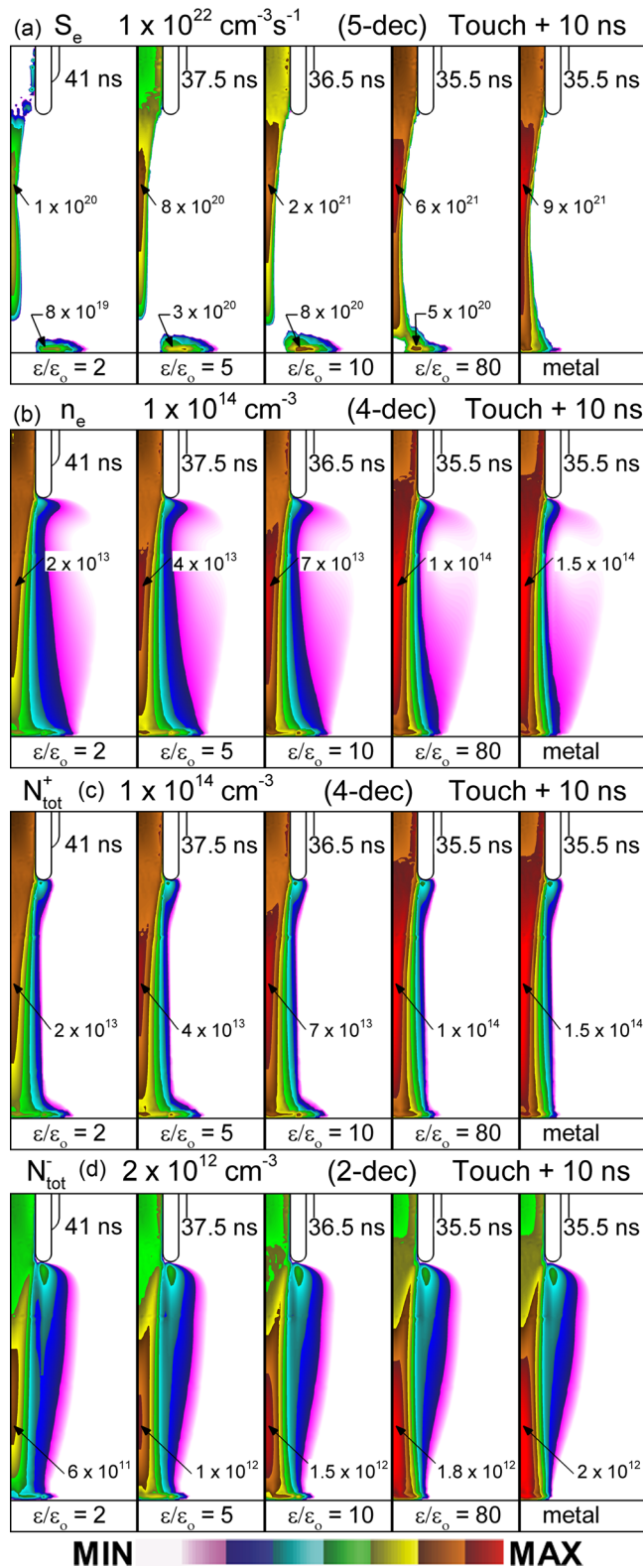


FIG. 4. Plasma dynamics at 10 ns after the ionization wave touches the material surface. From left to right, the frames correspond to relative permittivities of 2, 5, 10, and 80, and metal. The *touch* + 10 ns time is listed in each frame. (a) Electron impact ionization source  $S_e$ , (b) electron density, (c) total cation density, and (d) total anion density. Contours are on a log-scale with the maximum value and number of decades listed in the frame.

surface and a horizontal component of the electric field cannot be supported, at least at the surface. As a result, the SIW fails to significantly form. In this case, in the absence of a

ballast resistor, the full voltage remains across the gap. With increasing  $\epsilon_r$ , a transition occurs between two states. The first is surface charging, production of lateral electric fields and an SIW. The second is a fully sustained conduction channel and a restrike that eventually returns into the tube to connect with the electrode. At *touch* + 10 ns, the  $\epsilon_r = 80$  case combines the characteristics of the grounded case in which a fully developed plasma column connects the surface and the electrode, with the beginning of the formation of an SIW. As long as there is a finite capacitance, given a long enough voltage pulse, the surface will eventually charge, an SIW will eventually be formed and the  $S_e$  in the vertical column will eventually diminish. For example, for  $\epsilon_r = 80$ , the SIW separates from the vertical plasma column 17.5 ns after the impact of the ionization wave onto the dielectric.

At *touch* + 10 ns,  $n_e$  for  $\epsilon_r = 2$  is  $2 \times 10^{13} \text{ cm}^{-3}$ , and is nearly an order of magnitude lower than that for  $\epsilon_r = 80$  and for the metal substrate,  $1.5 \times 10^{14} \text{ cm}^{-3}$ . As  $\epsilon_r$  increases,  $n_e$  in the conductive channel increases. This increase in  $n_e$  is facilitated by the larger capacitance of the surface with increasing  $\epsilon_r$  that enables more conduction current to flow through the channel, and more displacement current through the dielectric, prior to charging of the capacitance. The lower  $n_e$  in the plasma columns with lower  $\epsilon_r$  is partially compensated by greater spread of the plasma on the dielectric facilitated by the SIW. However, the electron density in the SIW is 10–100 times smaller than that in the vertical plasma column. The grounded plate enables formation of a conduction channel unimpeded by charging of the surface, albeit at the loss of spreading of the discharge on the surface.

The density of cations (positive ions) follows that of the electrons with nearly identical values at this time in the discharge. That is, the anion (negative ion) density is small. At *touch* + 10 ns, the electrons and cations start to spread across the surface of the dielectric material, most clearly shown for  $\epsilon_r = 2, 5, \text{ and } 10$ , following the propagation of the SIW. The spread is most rapid in the  $\epsilon_r = 10$  case. In the plasma column at a distance of 3 mm from the exit of the dielectric tube, the cation having the highest density is  $\text{O}_2^+$ , comprising 54%, 49%, 48%, 43%, and 42% of the total cation density for  $\epsilon_r = 2, 5, 10, 80, \text{ and } \text{metal}$  surfaces.  $\text{O}_2^+$  is dominantly formed through direct electron impact ionization of  $\text{O}_2$  in the admixture or ambient or by the multistep ionization of  $\text{O}_2(^1\Delta)$  or  $\text{O}_2(^1\Sigma)$ . For example, near the He–air interface, ionization of the ground state of  $\text{O}_2$  accounts for 67% of the formation of  $\text{O}_2^+$  by electron impact, and multistep ionization of  $\text{O}_2(^1\Delta)$  or  $\text{O}_2(^1\Sigma)$  accounts for roughly a third. The next most prevalent cation is  $\text{N}_4^+$  formed from  $\text{N}_2^+$  in a three-body collision with  $\text{N}_2$  and another neutral.  $\text{N}_4^+$  comprises 40%, 37%, 36%, 36%, and 35% of the cations for  $\epsilon_r = 2, 5, 10, \text{ and } 80, \text{ and } \text{metal}$  surfaces. Along the surface, at the farthest extent of the spread of the SIW for  $\epsilon_r = 2, 5, \text{ and } 10$ ,  $\text{N}_4^+$  slightly exceeds  $\text{O}_2^+$  as the dominant cation. This reversal of the dominant cation results from the greater amount of mixing of ambient air with the He/ $\text{O}_2$  mixture flowing radially outward from the stagnation point on axis. This mixing increases the  $\text{N}_2$  density which promotes formation of  $\text{N}_4^+$ .

The density of cations generally decreases from the plasma column in the tube to the surface and into the SIW. However,

the density of anions increases as the surface is approached and increases with increasing permittivity. At 2 mm above the surface in the plasma column, the anion density increases from  $6 \times 10^{11} \text{ cm}^{-3}$  for  $\epsilon_r=2$ , to  $2 \times 10^{12} \text{ cm}^{-3}$  for the metal substrate. At this point in the development of the discharge (touch + 10 ns) and same location (2 mm above the surface), the dominant anion is  $\text{O}^-$  formed by dissociative attachment of  $\text{O}_2$ , and comprises 88%, 86%, 84%, 82%, and 82% of the anions for  $\epsilon_r=2, 5, 10$ , and 80, and metal.  $\text{O}_2^-$  comprises the majority of the remaining anions formed through three-body electron impact attachment. The  $\text{O}^-$  anion also dominates in the spread of the discharge along the surface with similar proportions.

Several key reactive species have been formed by electron impact excitation at this point in the discharge. The densities of  $\text{He}^*$ ,  $\text{O}$ ,  $\text{N}_2^*$ , and  $\text{OH}$  at touch + 10 ns are shown in Fig. 5.  $\text{He}^*$  represents the sum of the excited states of He included in the model. [ $\text{He}(2^1\text{S})$ ,  $\text{He}(2^1\text{P})$ ,  $\text{He}(2^3\text{S})$ ,  $\text{He}(2^3\text{P})$ ,  $\text{He}(3\text{S})$ , and  $\text{He}(3\text{P})$ .] At touch + 10 ns, the dominant excited state is the metastable  $\text{He}(2^3\text{S})$ , comprising between 50% and 33% of the  $\text{He}^*$  density from low to high permittivity. The production of  $\text{He}^*$  by electron impact with the helium feed gas has a minimum threshold energy of 19.8 eV for  $\text{He}(2^3\text{S})$ . As a result,  $\text{He}^*$  is dominantly formed in the high density, more energetic stream of electrons ( $T_e=3\text{--}4\text{ eV}$ ) which occurs along the wall of the discharge tube, and transitioning back to the axis of the plasma column near the exit of the tube. These excited states are important for subsequent Penning ionization and helium dimer formation. The propagation of the SIW is further shown by the concentration of  $\text{He}^*$  along the surface of the  $\epsilon_r=5, 10$ , and 80 materials.

The density of O atoms significantly increases with the increase in electron density in the conductive channel rising from  $1 \times 10^{14}$  to  $7 \times 10^{14} \text{ cm}^{-3}$  as the relative permittivity increases from 2 to 80 (and metal). The O atoms are formed from electron impact dissociation of  $\text{O}_2$  and react with  $\text{O}_2$  and another neutral in a three-body collision in the ambient or admixture to form  $\text{O}_3$ . The density of O atoms should increase with extension of the ionization wave further from the end of the tube into the plume where the density of  $\text{O}_2$  from the ambient is larger. This increase in O is somewhat tempered by the loss of O atoms in forming ozone, which also increases with  $\text{O}_2$  diffusing into the plume from the ambient. Also in the far-field, the O atoms collide with N atoms and another neutral to be a secondary source of NO, an important molecule for cell signaling.

The electronically excited  $\text{N}_2^*$ , representing the sum of the metastable  $\text{N}_2(\text{A}^3\Sigma)$  and  $\text{N}_2(\text{B}^3\Pi)$  states, is formed from electron impact with  $\text{N}_2$  (minimum threshold energy 6 eV) that has diffused into the helium channel. The density of  $\text{N}_2^*$  increases from  $9 \times 10^{14} \text{ cm}^{-3}$  to  $4\text{--}5 \times 10^{15} \text{ cm}^{-3}$  from  $\epsilon_r=2$  to 80 (and metal). The density of  $\text{N}_2^*$  is maximum on axis in spite of the  $\text{N}_2$  diffusing into the plume from larger radius because the ionization wave propagates on axis outside the tube where  $\text{N}_2$  is found.  $\text{N}_2^*$  provides another source of O atoms through dissociative excitation transfer collisions with  $\text{O}_2$ . The  $\text{N}_2^*$  also provides another source of NO through its reaction with O or  $\text{O}_3$ .

Similar to  $\text{N}_2^*$ , the hydroxyl radical, OH, is also dominantly formed from the interaction of the electrons on axis in

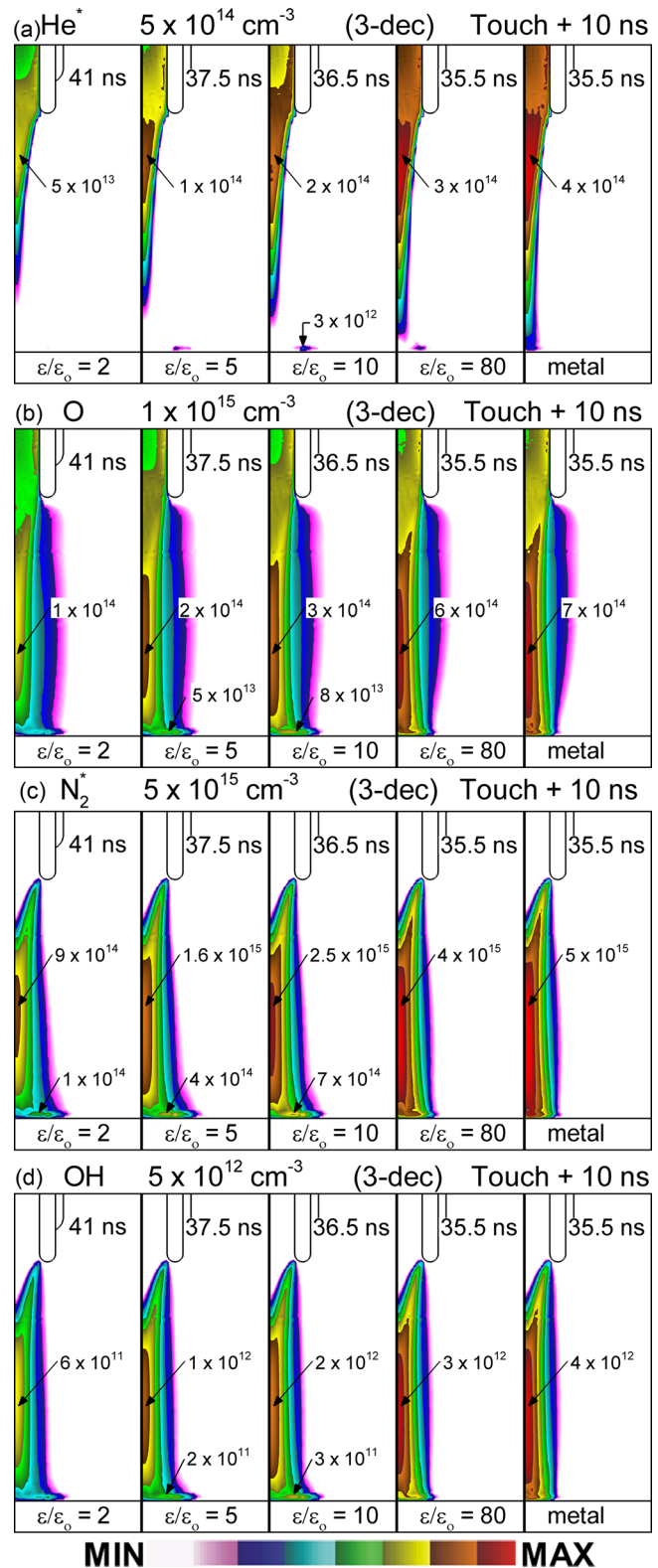


FIG. 5. Production of key neutrals at 10 ns after the ionization wave touches the material surface (touch + 10 ns). From left to right, the frames correspond to relative permittivities of 2, 5, 10, and 80, and metal. The times listed correspond to touch + 10 ns. (a)  $\text{He}^*$ , (b) O atoms, (c)  $\text{N}_2^*$ , and (d) OH. Contours are on a three decade log-scale from the maximum value listed in the frame.

the plume with  $\text{H}_2\text{O}$  diffusing into the plume. As a result, the spatial profiles of  $\text{N}_2^*$  and OH are similar. As OH accumulates, it combines with itself in a three-body reaction to form

H<sub>2</sub>O<sub>2</sub>. The lateral spread of the key neutrals along the material surface is best shown in  $\epsilon_r = 10$  frame of Fig. 5. The density accumulating on the surface is lower than that in the plasma channel at this point and follows the spread of the surface ionization wave and the electrons.

### C. End of maximum applied voltage 80 ns

Plasma properties [ $T_e$ ,  $n_e$ ,  $N_{\text{tot}}^+$  (cation density) and  $N_{\text{tot}}^-$  (anion density)] are shown in Fig. 6 at the end of the maximum applied voltage of the pulse at 80 ns. At this time, the low permittivity materials have nearly fully charged and removed voltage from the gap, resulting in the electric field in the gap being low. For example, at mid gap,  $E/N$  increases from 5 Td for  $\epsilon_r = 2$ , to 18 Td for  $\epsilon_r = 80$  (and metal). As a result, at mid gap,  $T_e$  increases from 1 eV for  $\epsilon_r = 2$ , to 2.8 eV for  $\epsilon_r = 80$  (and metal). In spite of the large range of  $T_e$  in the gap, the temperature is 3 eV throughout the extent of spread of the SIW. The spread of the SIW requires a minimum value of  $T_e$  regardless of the value of  $\epsilon_r$ . The  $\epsilon_r = 80$  case combines the two trends of increasing  $T_e$  in the plasma column and having a finite SIW. The maximum value of  $T_e$  in the conduction channel is 2.9 eV and in the SIW along the surface is 3 eV. Although the spatial distribution of  $n_e$  is less sensitive to  $\epsilon_r$ , the spatial distribution of  $T_e$  depends on  $\epsilon_r$ . Subsequently, the rates of formation and accumulation of the charged species on the different surfaces and in the conduction channel are largely influenced by  $T_e$ .

For all values of  $\epsilon_r$ , the electron density increases during the voltage pulse and is maximum at the end of the high voltage portion of the pulse at 80 ns. In the plasma channel, 2 mm from the end of the dielectric tube, the electron density increases from  $4 \times 10^{13} \text{ cm}^{-3}$  for  $\epsilon_r = 2$ , to  $7 \times 10^{14} \text{ cm}^{-3}$  for the metal substrate. The conductivity of the channel increases proportionally to the permittivity. The maximum density in the spread of electrons along the surface increases with permittivity as well from  $1.5 \times 10^{12} \text{ cm}^{-3}$  for  $\epsilon_r = 2$  to  $3 \times 10^{13} \text{ cm}^{-3}$  for  $\epsilon_r = 80$ . Although the peak electron density at the surface increases with increasing  $\epsilon_r$ , the spatial extent of the SIW decreases with increasing  $\epsilon_r$ .

The density of cations,  $N_{\text{tot}}^+$ , follows that of the electron density in the conductive channel increasing with increasing permittivity by an order of magnitude from  $\epsilon_r = 2$  ( $4 \times 10^{13} \text{ cm}^{-3}$ ) to  $\epsilon_r = 80$  ( $7 \times 10^{14} \text{ cm}^{-3}$ ). Similarly along the surface of the material, the maximum  $N_{\text{tot}}^+$  increases from  $2 \times 10^{12} \text{ cm}^{-3}$  to  $2 \times 10^{13} \text{ cm}^{-3}$  for  $\epsilon_r = 2$  to  $\epsilon_r = 80$ , while again the spatial extent decreases with increasing  $\epsilon_r$ . In the plasma channel,  $\text{O}_2^+$  is the dominant anion comprising 60–80% of the total cation density (higher percentage at lower  $\epsilon_r$ ) with  $\text{He}^+$  accounting for up to 20% of the cation density for  $\epsilon_r = 80$  and the metal substrate. In the lower permittivity cases ( $\epsilon_r = 2, 5$ , and 10),  $\text{N}_4^+$  is the second most prevalent cation contributing between 10 and 20% to the total. At the surface of the dielectric material, the cations are dominated by  $\text{O}_2^+$  with one to two orders of magnitude drop for the next most prevalent cation ( $\text{N}_4^+$ ). Over the length of the pulse, the higher rate coefficient for electron-ion recombination for  $\text{N}_4^+$  ( $1.4 \times 10^{-7} \text{ cm}^3 \text{ s}^{-1}$  at

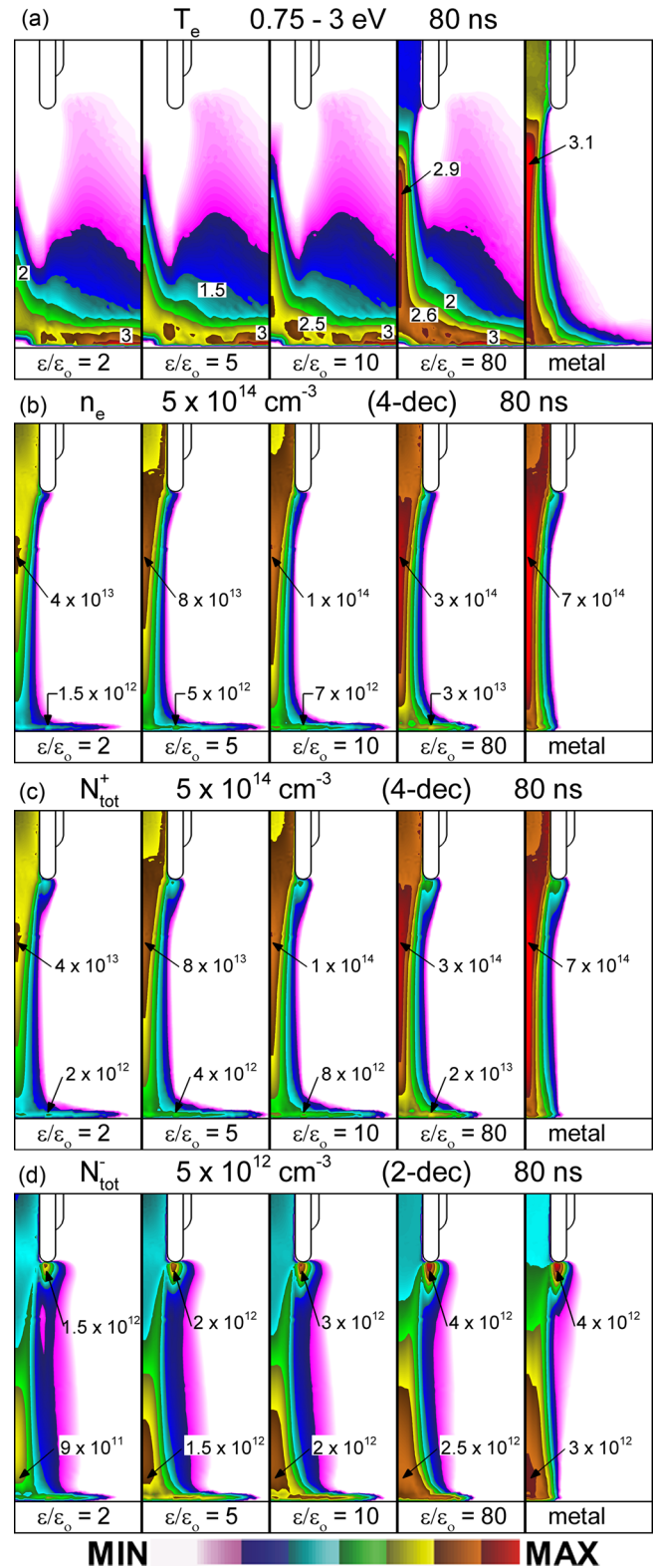


FIG. 6. Plasma dynamics at the end of the maximum applied voltage (80 ns). From left to right, the frames correspond to relative permittivities of 2, 5, 10, and 80, and metal. (a) Electron temperature  $T_e$  (linear scale from 1 to 3 eV), (b) electron density, (c) total cation density, and (d) total anion density. Contours for densities are on a log-scale with the maximum value and number of decades listed on the frame.

2 eV)<sup>33,34</sup> compared to  $7.3 \times 10^{-9} \text{ cm}^3 \text{ s}^{-1}$  (Refs. 35 and 36) for  $\text{O}_2^+$  at  $T_e = 2$  eV produces a decrease in  $\text{N}_4^+$  on the surface relative to  $\text{O}_2^+$ .

At the end of the high voltage portion of the discharge pulse, anions accumulate near the surface of the dielectric material and spread across the dielectric as they are formed by electron impact. This distribution of anions reflects the greater degree of diffusion of the ambient air into the plasma column and SIW, the further from the exit of the discharge tube. Unlike electrons and cations, the maximum density of anions occurs near the tip of the confining dielectric tube. At this location, a large density of low energy electrons is produced at the first interface of the He dominated plume with the ambient humid air. These low energy electrons then quickly attach to  $O_2$  forming  $O_2^-$ . Following the production of electrons, but with less dramatic increases, the range of anion density increases from  $1.5 \times 10^{12} \text{ cm}^{-3}$  for  $\epsilon_r=2$ , to  $4 \times 10^{12} \text{ cm}^{-3}$  for  $\epsilon_r=80$ . Along the surface,  $O^-$  is the dominant anion comprising  $6 \times 10^{11} \text{ cm}^{-3}$  of the total anion density of  $9 \times 10^{11} \text{ cm}^{-3}$  for  $\epsilon_r=2$ , or  $2/3$  of the total. For  $\epsilon_r=80$ , the density of  $O^-$  is  $2 \times 10^{12} \text{ cm}^{-3}$  of the total anion density of  $3 \times 10^{12} \text{ cm}^{-3}$ , also  $2/3$  of the total due to the values of  $T_e$  being similar in the SIW. The remainder of the anions is dominantly  $O_2^-$ .

The neutral species that will contribute to the production of the near-terminal reactive species (i.e.,  $O_3$ ,  $N_xO_y$ ,  $H_2O_2$ ) are shown in Fig. 7 at the end of the 80 ns high voltage portion of the discharge pulse. The lifetime of  $He^*$  against quenching by Penning ionization at mid-gap is 35 ns for  $\epsilon_r=2$ . So in the absence of continuous production,  $He^*$  can be depleted during the discharge pulse. As the  $E/N$  decreases in the plasma channel with decreasing  $\epsilon_r$ , the rate of production of  $He^*$  decreases and so the  $He^*$  is increasingly quenched in the absence of production. With increasing  $\epsilon_r$ , and increasing  $E/N$ , the rate of production of  $He^*$  is maintained and is competitive with quenching. The density of  $He^*$  at 80 ns increases from  $2 \times 10^{13} \text{ cm}^{-3}$  for  $\epsilon_r=2$ , to  $6 \times 10^{13} \text{ cm}^{-3}$  for  $\epsilon_r=80$ .

Over the 50 ns from the ionization wave touching the dielectric to the end of the high voltage discharge pulse, the densities of the remaining key neutrals, O,  $N_2^*$  and OH, increase both in the plasma channel and along the surface. In spite of initially being produced in the tube, the density of O increases in the conduction channel as the electrons and  $N_2^*$  accumulate, both dissociating  $O_2$  by either direct electron impact or excitation transfer. The highest density of O atoms,  $2 \times 10^{16} \text{ cm}^{-3}$ , is again with the metal substrate and increases by an order of magnitude from  $5 \times 10^{14} \text{ cm}^{-3}$  for  $\epsilon_r=2$ , to  $8 \times 10^{15} \text{ cm}^{-3}$  for  $\epsilon_r=80$ . The spread of O atoms along the surface is greater for  $\epsilon_r=2, 5$  and  $10$  compared to  $80$  due to the reduction in the SIW, but the largest density at the surface,  $2 \times 10^{15} \text{ cm}^{-3}$ , occurs for  $\epsilon_r=80$ . This spatial spread was observed by Yonemori and Ono who measured the radial distribution of O atoms in an APPJ incident on rat skin albeit with the effects of accumulation raising the density higher on the surface than in the plasma jet.<sup>37</sup>

The density of  $N_2^*$  increases by an order of magnitude from  $5 \times 10^{15} \text{ cm}^{-3}$  to  $5 \times 10^{16} \text{ cm}^{-3}$  for the metal substrate between touching + 10 ns to the end of the high voltage portion of the pulse at 80 ns. The density of  $N_2^*$  increases by a lesser degree over this time with lower permittivity. The charging of the dielectric and reduction in  $E/N$  (and  $T_e$ ) in

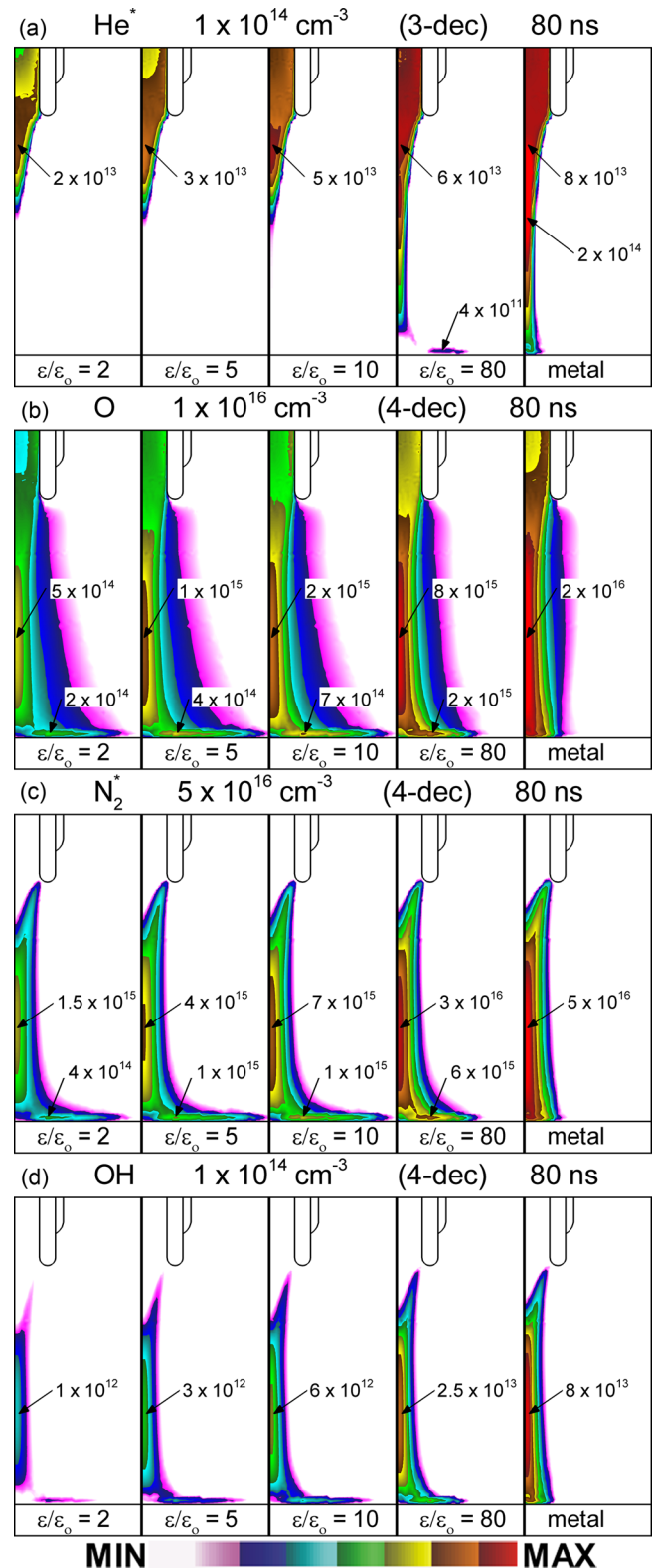


FIG. 7. Production of key neutrals at the end of the maximum applied voltage (80 ns). From left to right, the frames correspond to relative permittivities of 2, 5, 10, and 80, and metal. (a)  $He^*$  decreases in density compared to touch + 10 ns, (b) O atoms accumulate in the channel and on the surface, (c)  $N_2^*$  also accumulates in the channel and along the surface and (d) OH. Contours are on a log-scale with the maximum value and number of decades listed on the frame.

the plasma column with lower  $\epsilon_r$ , essentially terminates production of high threshold energy species, such as  $N_2^*$ . For the higher  $\epsilon_r$  and metal substrates, the continuing conduction

current (and restrike) maintains production of high threshold energy species for the duration of the discharge pulse. As in the distribution of ions, the tradeoff is in the spatial distribution of excited states. The conversion of conduction current in the plasma column into current in the SIW for low  $\epsilon_r$  results in a greater spatial extent of  $N_2^*$  along the surface, here maximizing for  $\epsilon_r=10$  to a distance of 3.9 mm. Although the spread of  $N_2^*$  is spatially more pronounced with lower permittivity, its density is higher at the surface ( $6 \times 10^{15} \text{ cm}^{-3}$ ) for  $\epsilon_r=80$ . Following the trends of  $N_2^*$ , the production of OH increased for all cases over the duration of the pulse (touching to 80 ns), nearly doubling to  $1 \times 10^{12} \text{ cm}^{-3}$  with  $\epsilon_r=2$  to increasing by a factor of 20 ( $8 \times 10^{13} \text{ cm}^{-3}$ ) for the metal substrate. This increase in OH density has been experimentally observed at a similar value ( $1 \times 10^{14} \text{ cm}^{-3}$ ) for a metal target by Riès *et al.*<sup>37</sup> The predicted OH density for the  $\epsilon_r=10$  case compares well with the measured OH density on axis above a glass surface observed by Yonemori and Ono.<sup>38</sup>

The charging of the dielectric removes voltage from the gap, thereby reducing Joule heating, electron density, and radical production in the plasma column. This voltage ultimately appears in the dielectric. The absence of a significant electric field in the conduction channel for  $\epsilon_r=2, 5,$  and  $10$  not only decreases the current density but also limits the Joule heating produced by these discharges. For example, the electric fields at the end of the high voltage discharge pulse are shown in the conduction channel and dielectric in Fig. 8. Increasing  $\epsilon_r$  decreases the voltage and the subsequent electric field propagation into material from 36 kV/cm for  $\epsilon_r=2$ , to 23 kV/cm for  $\epsilon_r=80$ . At a depth of 1 mm into the surface, or the bottom edge of Fig. 8(b), the magnitude of the electric field ranges from 28 kV/cm for  $\epsilon_r=2$ , to 13 kV/cm for  $\epsilon_r=80$ . Following the trend at touch + 10 ns, the potential drop across the dielectric is greatest for  $\epsilon_r=2$  at 10 kV decreasing to a penetration of potential of 3 kV for  $\epsilon_r=80$ .

The extent of the spread of the surface ionization wave and region of high electron temperature follow from the region of high electric field in the plasma above the material surface. In order to conserve current, the low dielectric constant material requires a larger time rate of change of the electric field leading to the higher electric fields in the material. This maintains the displacement current at the interface to be similar to the conduction currents through the plasma region. The metal target provides a direct path to ground for the conduction current without electric field enhancement at the surface.

#### D. End of voltage pulse (100 ns)

The formation of the plasma column in the atmospheric pressure guided streamer follows the same conceptual precepts as in a conventional low pressure glow discharge sustained in a dielectric tube. An ambipolar electric field is produced in the radial direction to confine the more mobile electrons and accelerate the less mobile positive ions to have equal radial fluxes. The end result is an electropositive plasma—a small net positive charge density in the plasma column. The majority of the positive charge resides at the

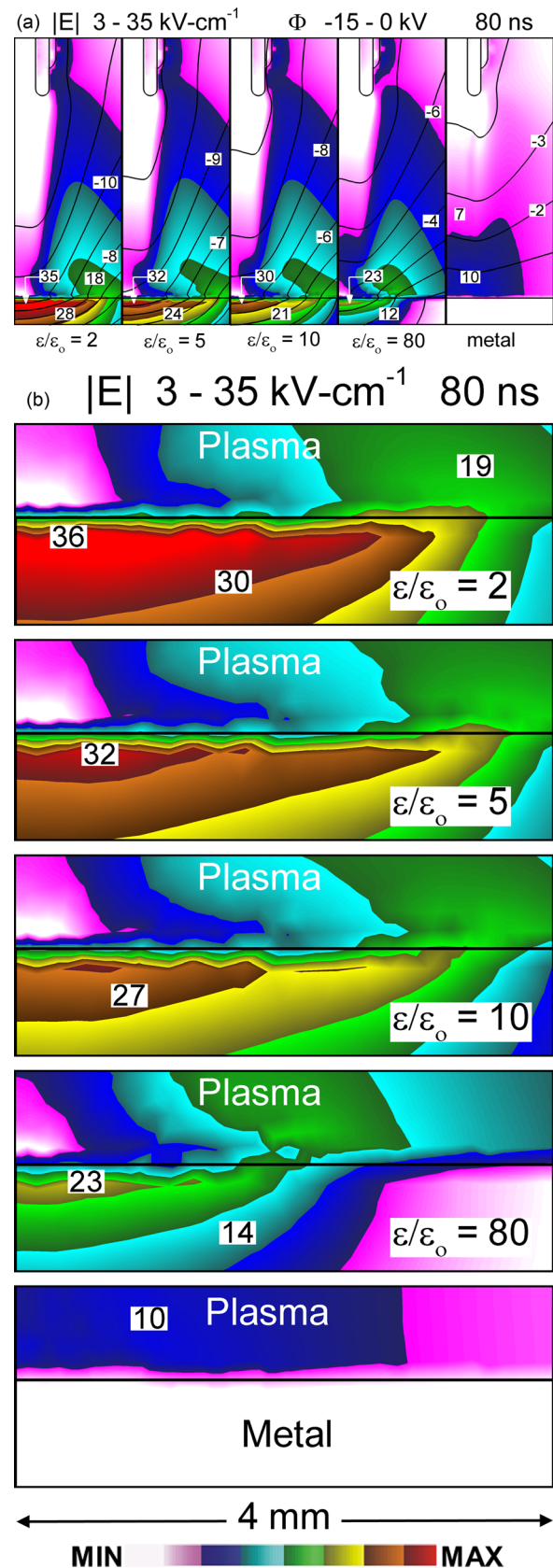


FIG. 8. Magnitude of the electric field at the end of the maximum applied voltage (80 ns). From left to right or top to bottom, the frames correspond to relative permittivities of 2, 5, 10, and 80, and metal. (a) The maximum extent of the penetration of the electric field into the dielectric, and electric potential contours at  $-1 \text{ kV}$  intervals. (b) Close up of the material surface showing the penetration of the electric field. Contours for the electric field are on a linear scale from 3 to 35 kV/cm.

edge of the plasma column where the ambipolar electric field is the largest. In a low pressure, glow discharge, the negative charge that balances the electropositive charge in the plasma column resides on the inside surface of the discharge tube. This negative charge results from the more mobile electrons that initially leave the plasma and so create the positive space charge. A similar process occurs in the atmospheric pressure guided streamer. However, since there is no tube on which the diffusing negative charge resides, the negative charge takes the form of a negative space charge layer bounding the positive space charge layer. Due to the streamer being bounded by the ambient air, the negative space charge layer is eventually dominated by negative ions as the low energy electrons attach to  $O_2$ . The negative ions are dominantly  $O_2^-$  near the exit of the tube where  $T_e$  is smaller, and transitioning at the midgap to  $O^-$  formed by dissociative attachment to  $O_2$  and attachment of low energy electrons to previously formed O atoms.

These trends are shown in Fig. 9 where the positive space charge, negative space charge, magnitude of the electric field, and electric potentials are shown at 100 ns, the termination of the voltage pulse, for  $\epsilon_r = 5$  and 80, and metal substrates. The electric fields and potentials, with enlargement of the plasma-dielectric interface, are shown in Fig. 10 for all cases. The boundary of the plasma column is defined by the positive space charge layer which itself is bounded by the balancing negative space charge layer. In between is the ambipolar electric field produced by this dipole-like structure. For that portion of the plasma column that is inside the tube, the positive space charge bounds the tube and the negative charge is largely on the tube.

As the voltage pulse falls from  $-15$  kV to 0 kV from 80 ns to 100 ns, most electrons in the boundary layer attach to form negative ions. The heavier cations remain in place and form an ion matrix. The resulting radial electric field is then largely sustained between the positive and negative ion matrices. As  $\epsilon_r$  increases, the magnitude of the ion matrix sustained electric field decreases from 34 kV/cm (132 Td) for  $\epsilon_r = 2$  to 19 kV/cm (73 Td) for  $\epsilon_r = 80$ . These trends in electric field are produced by a decreasing charge density bounding the plasma column. The maximum total positive charge is  $2 \times 10^{12} \text{ cm}^{-3}$  for  $\epsilon_r = 5$  compared to  $1 \times 10^{12} \text{ cm}^{-3}$  for  $\epsilon_r = 80$ . The balancing negative ion matrix has a lower peak density (for example,  $2 \times 10^{11} \text{ cm}^{-3}$  for  $\epsilon_r = 5$ ) due to its larger volume.

The charge balance and resulting electric fields are in some cases dominated by the surface charging. With the pin electrode inside the tube now at ground potential, the negative charge on the surface represents a negative voltage source which produces a  $-4$  to  $-5$  kV potential drop. The resulting electric fields are shown in Fig. 10(b). Here, the maximum magnitude of the electric field at the surface has the opposite trend of the electric field produced by the ion matrices in the gas phase. The local electric fields at the surface increase with increasing permittivity with these maxima having a smaller spatial extent. A larger charge accumulates on the higher capacitance, higher permittivity materials as shown in Fig. 6. When the applied voltage is removed, this larger accumulated charge produces a larger electric field at the surface in the gas. As shown in Fig. 10(b), increasing

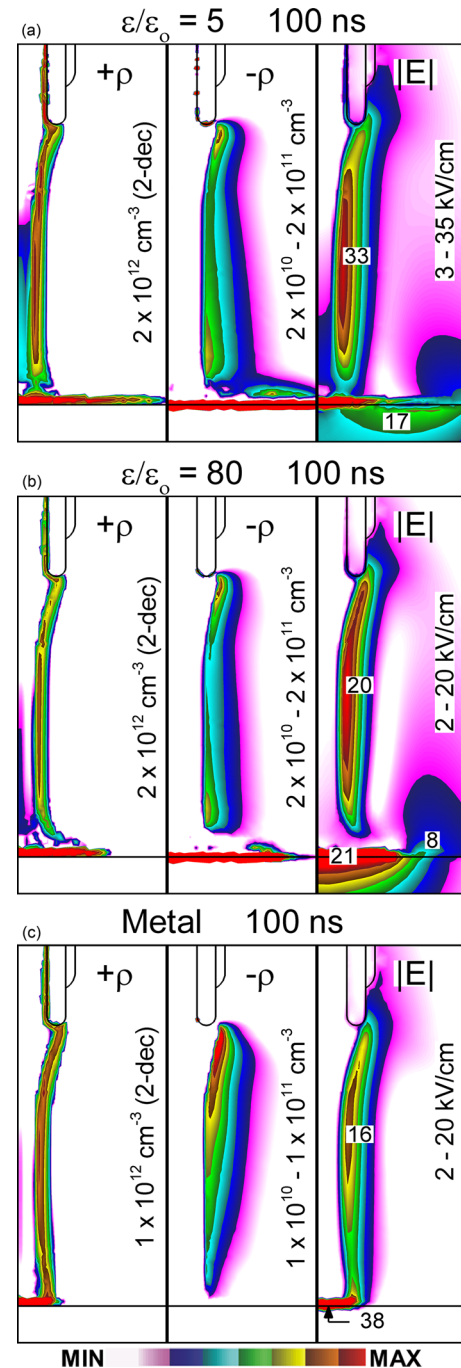


FIG. 9. Total positive and negative charge densities, and resulting electric field (with voltage contours) when the applied voltage pulse returns to 0 at 100 ns. (a)  $\epsilon_r = 5$  (tissue-like), (b)  $\epsilon_r = 80$  (water-like), and (c) metal. For positive charge density, contours are on a log-scale with the maximum value and number of decades listed on the frame. For negative charge density and magnitude of the electric field, the contours are on a linear scale for the range of values listed.

permittivity increases the magnitude of the surface electric field from 40 kV/cm (170 Td) for  $\epsilon_r = 2$  to 108 kV/cm (400 Td) for  $\epsilon_r = 80$ .

The distribution of charge in the vicinity of the surface has two components, as shown in Fig. 11 for  $\epsilon_r = 5$  and 80, and for the metal. There is negative charge deposited on the surface of the material and positive space charge density in the plasma above the surface. The positive space charge results from a positive-ion matrix sheath—the more mobile

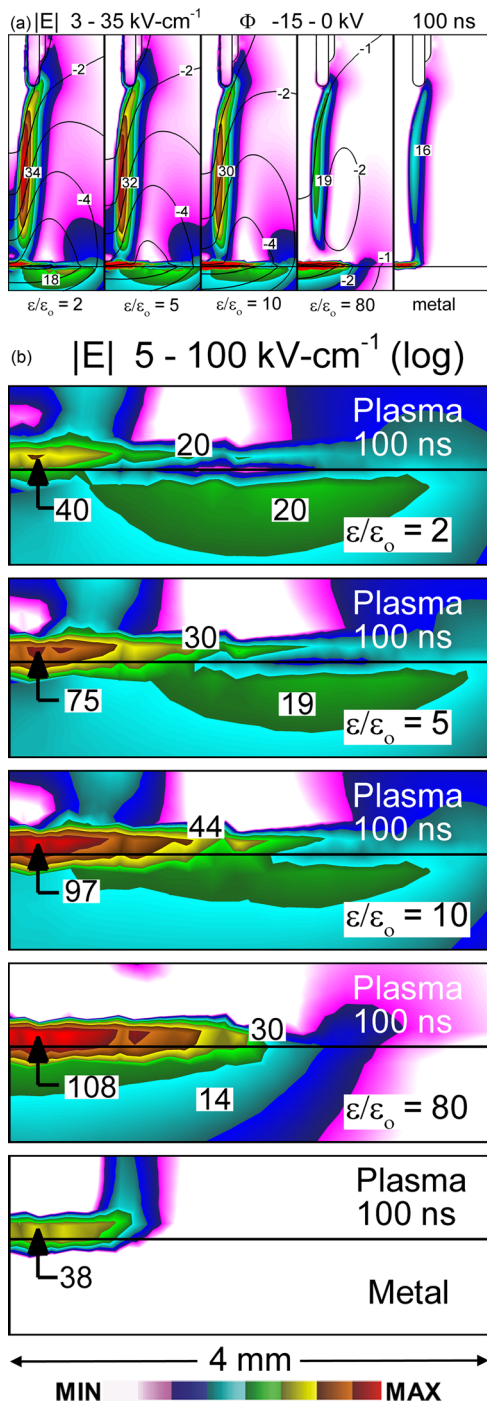


FIG. 10. Magnitude of the electric field at the end of the applied voltage (100 ns). From left to right or top to bottom, the frames correspond to relative permittivities of 2, 5, 10, and 80, and metal. (a) The resulting ion matrix and surface electric fields resulting from the charge separation when the applied voltage returns to 0. Contours are on a linear scale from 3 to 35 kV/cm. The potential contours at  $-1$  kV intervals. (b) Close up of the electric field at the material surface. Contours are on a log-scale from 5 to 100 kV/cm.

electrons flowed from this region into the surface leaving behind the ion matrix sheath. For the low permittivity case ( $\epsilon_r=5$ ), the smaller RC time constant for charging the surface and the more rapid spread of negative charge produces comparable charge densities on the surface (negative) and in the sheath (positive). The end result is a lower intensity electric field 75 kV/cm (286 Td). The high permittivity case ( $\epsilon_r=80$ ) has nearly an order of magnitude lower positive

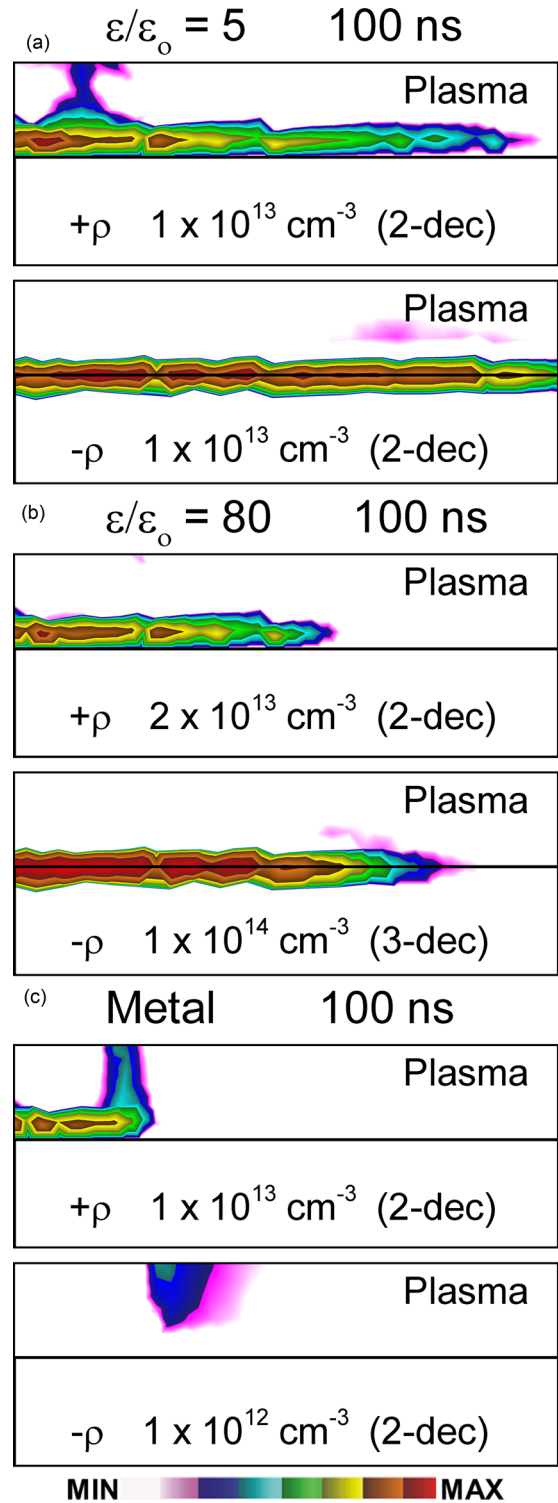


FIG. 11. An enlarged view of the material surface showing total positive (top frame) and negative charge densities (bottom frame) that result in a surface electric field. The time is 100 ns when the applied voltage pulse returns to 0. (a)  $\epsilon_r=5$  (tissue-like), (b)  $\epsilon_r=80$  (water-like), and (c) metal. Contours are on a log-scale with the maximum value and number of decades listed on the frame.

charge density ( $2 \times 10^{13}$  cm<sup>-3</sup>) in the ion matrix sheath compared to the negative charge ( $1 \times 10^{14}$  cm<sup>-3</sup>) on the surface. This situation results from electron current flowing through the ion matrix sheath to the surface to charge the larger capacitance. This large imbalance produces an electric field of 108 kV/cm. The positive charge density does increase

with  $\epsilon_r = 80$  compared to  $\epsilon_r = 5$  due to the larger electron current density producing more ionization in the sheath. However, the negative charge density on the surface increases by an order of magnitude from  $1 \times 10^{13} \text{ cm}^{-3}$  for  $\epsilon_r = 5$  to  $1 \times 10^{14} \text{ cm}^{-3}$  for  $\epsilon_r = 80$  due to the flow of electron current through the sheath to charge the capacitance. The negative charge extends further along the surface than does the positive charge, a consequence of the negative SIW that is sustained by negative space charge at its leading edge.

These trends apply to non-conducting material which translate to an infinite dielectric relaxation time,  $\epsilon/\sigma$ . Materials with finite conductivities and a finite dielectric relaxation time will dissipate the surface charge. At one extreme, the metal does not accumulate surface charge because that charge is virtually instantly dissipated. The electric field produced at the surface of the metal substrate is due to an anode sheath created by the accumulation of positively charged species near the surface as the electrons flow into the metal. The negative charge that extends from above into the frame of Fig. 11(c) for the metal surface is from the lower extent of the anions that forms the ion-matrix, ambipolar, electric field that confines the plasma column. It is not due to surface charging.

#### IV. CONCLUDING REMARKS

By changing only the relative permittivity of the material upon which an APPJ is directed, significant effects on the dynamics of the discharge, production of charged and reactive species, and the behavior of the electric field are realized. Increasing the permittivity increases the speed of the ionization wave to the surface, increases the electron density and subsequent ion density in the plasma column. The larger electron density and higher electron temperature in the conduction channel and at the surface of the high permittivity materials over the pulse duration increase the production of key neutrals of interest to biological applications created by the discharge. A lower permittivity enables greater spread of the plasma along the surface by propagation of the surface ionization wave, and allows more penetration of the electric field into the material.

By using a pulse length of 80 ns for the maximum applied voltage, we believe that we have captured the unique properties of APPJs when transitioning from low-to-high permittivity substrates. For example, with low permittivity materials, the electric field penetrates completely into the material and the SIW is well established. For pulse lengths longer than 80 ns with low  $\epsilon_r$ , we expect the SIW to continue to spread until the applied voltage is insufficient to generate the avalanche electric field at the head of the SIW, at which time it will quench. There will be little gas heating. For longer pulses with high  $\epsilon_r$  materials, the dielectric will eventually charge, which will launch more aggressive SIWs. The higher currents during this time will produce greater gas heating. With the metal substrate, a glow to arc transition will eventually occur.

The dynamics of the fall of the voltage pulse revealed that the development of an ion matrix electric field at the edge of the conductive channel, and the electric field at the surface was influenced by the permittivity of the material as

well. The ion matrix produced ambipolar electric field surrounding the plasma column is larger for lower permittivity materials and is produced from the greater number of negatively charged species remaining in the plasma region. The electric field remaining at the surface resulting from electron charging increases with increasing permittivity.

#### ACKNOWLEDGMENTS

This work was supported by the Department of Energy Office of Fusion Energy Science (DE-SC0001319) and the National Science Foundation (CHE-1124724).

- <sup>1</sup>A. Schutze, J. Jeong, S. Babayan, J. Park, G. Selwyn, and R. Hicks, "The atmospheric-pressure plasma jet: A review and comparison to other plasma sources," *Trans. Plasma Sci.* **26**, 1685 (1998).
- <sup>2</sup>M. G. Kong, G. Kroesen, G. Morfill, T. Nosenko, T. Shimizu, J. van Dijk, and J. L. Zimmerman, "Plasma medicine: An introductory review," *New J. Phys.* **11**, 115012 (2009).
- <sup>3</sup>M. Laroussi, "Low-temperature plasmas for medicine?," *Trans. Plasma Sci.* **37**, 714 (2009).
- <sup>4</sup>M. Laroussi, I. Alexeff, and W. Kang, "Biological decontamination by non-thermal plasmas," *IEEE Trans. Plasma Sci.* **28**, 184 (2000).
- <sup>5</sup>M. Laroussi, M. Kong, G. Morfill, and W. Stolz, *Plasma Medicine: Applications of Low-Temperature Gas Plasmas in Medicine and Biology* (Cambridge University Press, Cambridge, 2012), pp. 156–174.
- <sup>6</sup>M. Keidar, *Plasma Source Sci. Technol.* **24**, 033001 (2015).
- <sup>7</sup>M. Keidar, A. Shashurin, O. Volotskova, M. Stepp, P. Srinivasan, A. Sandler, and B. Trink, "Cold atmospheric plasma in cancer therapy," *Phys. Plasmas* **20**, 057101 (2013).
- <sup>8</sup>K. Fricke, H. Steffen, T. von Woedtke, K. Schroder, and K.-D. Weltman, "High rate etching of polymers by means of an atmospheric pressure plasma jet," *Plasma Process. Polym.* **8**, 51 (2011).
- <sup>9</sup>C. van Gils, S. Hofmann, B. Boekema, R. Brandenburg, and P. Bruggeman, "Mechanisms of bacterial inactivation in the liquid phase induced by a remote RF cold atmospheric pressure plasma jet," *J. Phys. D: Appl. Phys.* **46**, 175203 (2013).
- <sup>10</sup>P. Bruggeman and C. Leys, "Non-thermal plasmas in and in contact with liquids," *J. Phys. D: Appl. Phys.* **42**, 053001 (2009).
- <sup>11</sup>J. Y. Jeong, S. E. Babayan, V. J. Tu, J. Park, I. Henins, R. F. Hicks, and G. S. Selwyn, "Etching materials with an atmospheric pressure plasma jet," *Plasma Sources Sci. Technol.* **7**, 282 (1998).
- <sup>12</sup>H. Paetzelt, G. Bohm, and T. Arnold, "Etching of silicon surfaces using atmospheric plasma jets," *Plasma Sources Sci. Technol.* **24**, 025002 (2015).
- <sup>13</sup>E. Robert, T. Darny, D. Ries, S. Dozias, and J.-M. Pouvesle, "Non thermal plasma jets interacting with targets and gas flows," in 67th Gaseous Electronics Conference (GEC), BAPS.2014.GEC.ET1.6, Raleigh, NC, 2–7 November 2014.
- <sup>14</sup>E. Robert, V. Sarron, T. Darny, D. Ries, S. Dozias, J. Fontane, L. Joly, and J.-M. Pouvesle, "Rare gas flow structuration in plasma jet experiments," *Plasma Sources Sci. Technol.* **23**, 012003 (2014).
- <sup>15</sup>D. Breden and L. L. Raja, "Computational study of the interaction of cold atmospheric helium plasma jets with surfaces," *Plasma Sources Sci. Technol.* **23**, 065020 (2014).
- <sup>16</sup>J. M. Strobel, M. Strobel, C. S. Lyons, C. Dunatov, and S. J. Perron, "Aging of air-corona-treated polypropylene film," *J. Adhes. Sci. Technol.* **5**, 119 (1991).
- <sup>17</sup>I. Ermolina, Y. Polevaya, Y. Feldman, B. Ginzburg, and M. Schlesinger, "Study of normal and malignant white blood cells by time domain dielectric spectroscopy," *Trans. Dielectr. Electr. Insul.* **8**, 253 (2001).
- <sup>18</sup>Y. Feldman, I. Ermolina, and Y. Hayashi, "Time domain dielectric spectroscopy study of biological systems," *Trans. Dielectr. Electr. Insul.* **10**, 728 (2003).
- <sup>19</sup>S. Norberg, E. Johnsen, and M. J. Kushner, "Formation of reactive oxygen and nitrogen species by repetitive negatively pulsed helium atmospheric pressure plasma jets propagating into humid air," *Plasma Sources Sci. Technol.* **24**, 035026 (2015).
- <sup>20</sup>S. Norberg, Ph.D. thesis (Department of Mechanical Engineering, University of Michigan at Ann Arbor, 2015).

- <sup>21</sup>X. Lu, M. Laroussi, and V. Puech, "On atmospheric-pressure non-equilibrium plasma jets and plasma bullets," *Plasma Sources Sci. Technol.* **21**, 034005 (2012).
- <sup>22</sup>X. Lu, Z. Jiang, Q. Xiong, Z. Tang, X. Hu, and Y. Pan, "An 11 cm long atmospheric pressure cold plasma plume for applications of plasma medicine," *Appl. Phys. Lett.* **92**, 081502 (2008).
- <sup>23</sup>E. Karakas, M. Akman, and M. Laroussi, "The evolution of atmospheric-pressure low-temperature plasma jets: Jet current measurements," *Plasma Sources Sci. Technol.* **21**, 034016 (2012).
- <sup>24</sup>S. Reuter, J. Winter, A. Schmidt-Bleker, H. Tresp, M. Hammer, and K.-D. Weltmann, "Controlling the ambient air affected reactive species composition in the effluent of an argon plasma jet," *Trans. Plasma Sci.* **40**, 2788 (2012).
- <sup>25</sup>H. D. Young and R. A. Freedman, *Sears and Zemansky's University Physics with Modern Physics*, 13th ed. (Addison-Wesley, San Francisco, 2012), p. 801.
- <sup>26</sup>S. Gabriel, R. W. Lau, and C. Gabriel, "The dielectric properties of biological tissues: III. Parametric models for the dielectric spectrum of tissues," *Phys. Med. Biol.* **41**, 2271 (1996).
- <sup>27</sup>A. Laughton and D. F. Warne, *Electrical Engineer's Reference Book*, 16th ed. (Butterworth & Co, London, 2002), p. 6/4.
- <sup>28</sup>C. Bogey and C. Bailly, in *Direct and Large-Eddy Simulation VII: Proceedings of the Seventh International ERCOFTAC Workshop on Direct and Large Scale Eddy Simulation VII*, edited by V. Armenio, B. Geurts, and B. Frohlich (Springer Science, 2010).
- <sup>29</sup>M. Teschke, J. Kedzierski, E. G. Finantu-Dinu, D. Korzec, and J. Engemann, "High-speed photographs of a dielectric barrier atmospheric pressure plasma jet," *Trans. Plasma Sci.* **33**, 310 (2005).
- <sup>30</sup>J. S. Sousa, K. Niemi, L. J. Cox, Q. Th. Algwari, T. Gans, and D. O'Connell, "Cold atmospheric pressure plasma jets as sources of singlet delta oxygen for biomedical applications," *J. Appl. Phys.* **109**, 123302 (2011).
- <sup>31</sup>S. Cellestin, G. Canes-Boussard, O. Guaitella, A. Bourdon, and A. Rousseau, "Influence of the charges deposition on the spatio-temporal self-organization of streamers in a DBD," *J. Phys. D: Appl. Phys.* **41**, 205214 (2008).
- <sup>32</sup>S. Cellestin, Z. Bonaventura, O. Guaitella, A. Rousseau, and A. Bourdon, "Influence of surface charges on the structure of a dielectric barrier discharge in air at atmospheric pressure: Experiment and modeling," *Eur. Phys. J. Appl. Phys.* **47**, 22810 (2009).
- <sup>33</sup>R. Dorai, Ph.D. thesis (Department of Chemical Engineering, University of Illinois at Urbana-Champaign, 2002).
- <sup>34</sup>J. B. A. Mitchell, "The dissociative recombination of molecular ions," *Phys. Rep.* **186**, 215 (1990).
- <sup>35</sup>D. S. Stafford and M. J. Kushner, " $O_2(^1\Delta)$  production in He/O<sub>2</sub> mixtures in flowing low pressure plasmas," *J. Appl. Phys.* **96**, 2451 (2004).
- <sup>36</sup>B. F. Gordiets, C. Ferreira, V. Guerra, J. Loureiro, J. Nahorny, D. Pagnon, M. Touzeau, and M. Vialle, *Trans. Plasma Sci.* **23**, 750 (1995).
- <sup>37</sup>D. Ries, G. Dilecce, E. Robert, P. F. Ambrico, S. Dozies, and J.-M. Pouvesle, "LIF and fast imaging plasma jet characterization relevant for NTP biomedical applications," *J. Phys. D: Appl. Phys.* **47**, 275401 (2014).
- <sup>38</sup>S. Yonemori and R. Ono, "Flux of OH and O radicals onto a surface by an atmospheric-pressure helium plasma jet measured by laser-induced fluorescence," *J. Phys. D: Appl. Phys.* **47**, 125401 (2014).